



Improved Etch Characteristics of Magnetic Tunneling Junction Materials by Using Helium

Sungwoo Park,^{a,*} Kyungchae Yang,^{a,*} Hoseok Lee,^b Dongwoo Kim,^a Jongung Baek,^c Taehun Shim,^c Jeagun Park,^c and Geunyoung Yeom^{a,b,z}

^aSchool of Advanced Materials Science and Engineering, Sungkyunkwan University, Suwon-si 16419, Korea

^bSKKU Advanced Institute of Nano-Technology (SAINT), Sungkyunkwan University, Suwon-si 16419, Korea

^cDepartment of Electronics Engineering, Hanyang University, Seoul 133-791, Korea

The etch characteristics of magnetic tunneling junction (MTJ) materials for spin transfer torque magnetic random access memory (STT-MRAM) using He inductively coupled plasma (ICP) were compared with the etch characteristics of ICP using Ar or CO/NH₃ (1:3). The ICP etching using He showed a higher etch selectivity of CoFeB over W and a more anisotropic etch profile compared to the etching using Ar at similar etch rates. The sputter etch characteristics of CoFeB and W were also investigated using the Stopping and Range of Ions in Matter (SRIM) simulation program. The results showed higher sputter etch selectivity of CoFeB over W in addition to narrower angular distribution of the sputtered atoms than those obtained using Ar. The etching of MTJ materials using CO/NH₃ (1:3) ICP exhibited good MTJ etch characteristics comparable to He ICP, however, the MTJ etched using CO/NH₃ (1:3) showed the lowest saturation magnetization (M_S) measured by a vibrating-sample magnetometer (VSM) possibly due to the sidewall oxidation of MTJ while the M_S values of the MTJ etched using He and Ar are similar. It is found that, by etching the MTJ materials using He ICP with the ion energy near the hardmask sputter threshold energy, highly anisotropic etch profiles could be obtained without forming the sidewall redeposited materials and without significant degradation of magnetic properties.

© 2017 The Electrochemical Society. [DOI: [10.1149/2.0151709jss](https://doi.org/10.1149/2.0151709jss)] All rights reserved.

Manuscript submitted June 29, 2017; revised manuscript received August 2, 2017. Published August 16, 2017. This was Paper 1018 presented at the New Orleans, Louisiana, Meeting of the Society, May 28-June 1, 2017.

As next generation memory devices replace volatile dynamic random access memory (DRAM) devices, many research groups in the semiconductor industry are investigating new nonvolatile memory devices like spin transfer torque magnetic random access memory (STT-MRAM), resistive random access memory (ReRAM), phase change random access memory (PRAM), etc.¹ Among these, STT-MRAM has many advantages such as high speed of read/write cycles, low power consumption of the device, and high density memory cells in addition to the nonvolatility of information.²⁻⁴ However, it is difficult to etch magnetic materials chemically and to etch small features such as a 20 nm thick magnetic tunneling junction (MTJ) because of sidewall redeposition and plasma induced etch damage. In addition, the sidewall re-deposition causes an electrical short and a tapered profile.⁵⁻¹¹

Ar ion milling (or Ar ion beam etch (IBE)) has been used to etch MTJ materials.¹²⁻¹⁴ The advantage of the Ar ion milling is that the process induces very little or no chemical damage to the MTJ materials. To improve the etch profile and to remove the sidewall redeposition, a side-milling process (etching by tilting) has been applied. But this can induce a shadow effect caused by adjacent cells in the case of high density MRAM with an aggressive pitch array, and which results in an electrical short failure due to the conductive redeposition at the edge of the pattern sidewall.¹⁵⁻¹⁷ Etching of MTJ materials using halogen-based etch gases such as Ar/Cl₂ chemistry in ICP reactive ion etching (ICP-RIE) systems has been reported to etch MTJ with little sidewall re-deposition.¹⁸ However, the etching using halogen gases involves lower etch selectivities over mask materials such as W and the formation of a thin halogenated surface layer induces corrosion.⁵ To avoid corrosion, ICP-RIE using C-O-based chemistry (CO/NH₃, CH₃OH, etc.) has been investigated.^{7,9,19-28,31} These noncorrosive gases yield possibly noncorrosive metal volatile compounds with transition metals.^{21,22} In addition, these gases give high etch selectivity due to oxidation, carbonization, and nitration of a hardmask surface.²⁷ However, oxygen in the gas chemistry tends to induce chemical damage on the MTJ material surface during the etching and form a thin oxide layer on the patterned sidewall of MTJ materials, which reduces the performance of the device, even though the oxide layer can be partially removed using a H₂ plasma.^{10,28-32}

In this study, to overcome the processing related problems described above, we investigated ICP etch characteristics using He gas

with the ion energy close to the sputter threshold energy of the hardmask. We etched MTJs with 55 nm width pillar type pattern. He gas was chosen as the etch gas because it has a larger threshold energy difference between the hardmask and materials to be etched than Ar due to its low energy transfer rate to the hardmask material. Therefore, it is also easier to improve the etch selectivity over the mask materials in addition to avoiding oxidation of the etched MTJ features. The MTJ etch characteristics using the ICP with He and Ar were compared with the SRIM simulation results on the sputter etching of magnetic materials using Ar and He to investigate the MTJ etch mechanism by He gas. The MTJ etch characteristics were also compared with the etch characteristics using CO/NH₃ (1:3) which showed high etch rates and highly anisotropic etch profiles in previous studies.^{11,33}

Experimental

All experiments were conducted using a commercially available radio frequency ICP etch system (STS PLC). Separate 13.56 MHz power generators were applied to both the ICP source and the bias electrode. The schematic diagram of the ICP etch system is shown in Fig. 1. For all experiments, the process conditions were kept at 700 W ICP power, 7 mTorr operating pressure, and 50 sccm gas flow rate. In the case of CO/NH₃, the gas mixture containing 12.5 sccm CO and 37.5 sccm NH₃ was used.

Blank unit thin film samples such as CoPt, MgO, CoFeB, and W that consist MTJ were etched with He, Ar, and CO/NH₃ gases using an ICP etch system and the etch rates and selectivities of the MTJ materials over W were calculated. Patterned MTJ samples were etched using He, Ar, and CO/NH₃ gas to observe the etch profiles and magnetic degradation. The patterned MTJ sample was composed of CoFeB(10nm)/MgO (1nm)/CoPt (10nm) on Ta/SiO₂/silicon wafer with a hard mask consisting of patterned W (100 nm)/Ti (3 nm)/Ru (10 nm). The half pitch of the pattern was 55 nm.

The etch depths were measured using a step profiler and field emission scanning electron microscopy (FE-SEM; Hitachi, S-4700) for blank unit films and also by FE-SEM for patterned samples. The etch profiles were observed using the FE-SEM and transmission electron microscopy (Cs-corrected TEM; JEOL JEM, ARM 200F). The patterned MTJ samples which were cut into 1 cm × 2 cm pieces were analyzed with a vibrating sample magnetometer (VSM; GMW, 3474-140) to measure the magnetic hysteresis curves at room temperature, and, therefore, to identify magnetic degradation of the MTJ samples etched by He, Ar, and CO/NH₃ (1:3) gases. In this 1 cm × 2 cm MTJ coupon, a series of MTJ pattern which can

*These authors contributed equally to this work.

^zE-mail: gyeom@skku.edu

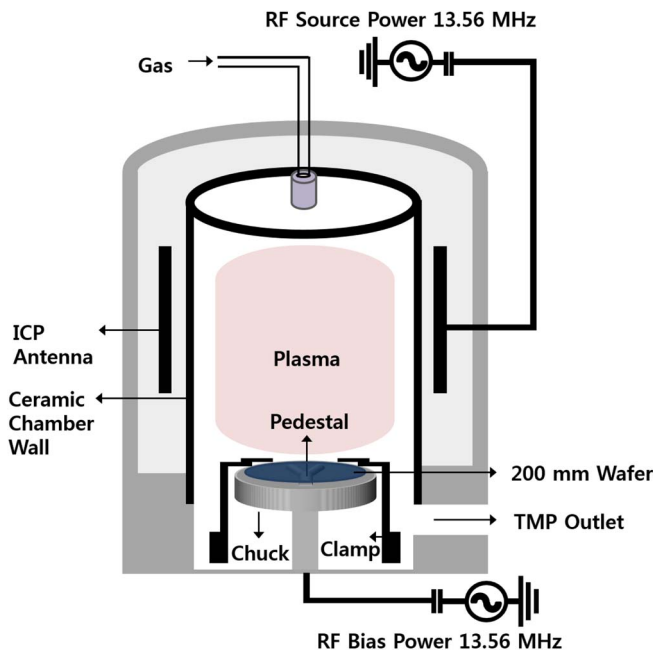


Figure 1. Schematic of the ICP reactive ion etch system used in the experiment.

measure M-H property of MTJ features are located and this MTJ pattern in the $1\text{cm} \times 2\text{ cm}$ coupon is repeated in the wafer, so, we cut the same MTJ pattern and used for the VSM measurement to obtain M-H properties more reliably.

SRIM simulation was conducted to investigate the sputter yield $\langle S \rangle$ ($\langle S \rangle = (\text{sputtered atom})/(\text{incident sputter ion})$) of CoFeB and the sputter etch selectivity over W during sputter etching using He and Ar ion, and to investigate the similarity between the simulation results and the actual etch data. Co and Fe have a combined mole fraction of 0.8 in CoFeB (4:4:2) used in this study. Therefore, the sputter yields of Co and Fe were used for the final sputter yield calculation of CoFeB because the sputter etch rates of these elements have close relation with the etch rate of CoFeB. W was also used as mask material for the simulation. The specific simulation conditions are described in Table I. The monolayer collision steps/surface sputtering calculation mode was used. Analyses such as sputter etch selectivity, sputtered atomic angle, and energy distribution of sputtered atoms were performed using the SRIM data.³⁶

Results and Discussion

First, the sputter yields of Co, Fe, and B in CoFeB were calculated using the SRIM program with the conditions in Table I and the results are shown in Table II. It was reported by Wehner and et al.³⁷ that the sputter threshold energy of W by He is in the range of 100~200 eV, hence, to maximize the etch selectivity between CoFeB and W, the He ion energy from 150 to 350 eV was used in the sputter etch simulation. For the Ar ion energy, the energy ranges from 35 to 52 eV, which showed a similar sputter etch rate range of CoFeB to that by He ions, was used in the simulation. Sputtering yield means the number of atoms sputtered by one He or Ar atom. Therefore, 0.036 means that one He atom causes the ejection of 0.036 atom from the CoFeB layer. As shown in Table II, at 150 eV of He ion energy, the sputter yields of Co and Fe were similar as 0.036; and these values were similar to the sputter yields of Co (0.037) and Fe (0.036) at the Ar ion energy of 35 eV. Therefore, Co and Fe in CoFeB exhibit almost similar sputter yields for both He and Ar. However, in the case of the sputter yield of W, the sputter yield with 35 eV Ar was much higher than that with 150 eV He; therefore, the sputter yield ratio of CoFeB/W for He was much higher than that for Ar, while having similar sputter yield values of CoFeB. Similar results were obtained for 250 eV He/47 eV Ar and for 350 eV He/52 eV Ar. The increase of He ion energy (150, 250, 350 eV) increased the CoFeB sputter yield values, but the sputter yield ratio of CoFeB/W decreased from ~600 at 150 eV to ~34 at 250 eV, and to ~3 at 350 eV He together with the decreased sputter yield ratio of CoFeB/W for Ar from ~6.7 at 35 eV to ~0.9 at 47 eV, and to ~0.7 at 52 eV. The higher sputter yield ratio of CoFeB/W for He compared to Ar was related to the lower energy transfer rate (T) to W from He compared to Ar because the elastic energy transfer between the two atoms can be expected from the following formula;

$$T = \frac{4 \times Mm}{(M + m)^2} E \quad [1]$$

where, M is the mass of the target atom, m is the mass of the incident atom, and E is the energy of the incident atom. The energy transfer rates of Co/Fe and W by He, Ne, Ar, and Xe were compared using Eq. 1 and the results on the energy transfer rate and their ratios of (Co/Fe)/W are shown in Fig. 2. As shown in the figure, the use of higher mass incident atom increased the energy transfer rate for both Co/Fe and W, which results in the increase of sputter yield, but the energy transfer rate ratio of (Co/Fe)/W was decreased with increasing the gas atomic mass indicating the decreased sputter yield ratio. To maximize the sputter etch selectivity between MTJ material and W hardmask and to decrease damage, it is found that a sputter etch gas with lower atomic weight which results in higher energy transfer rate ratio of CoFeB/W is required.

Table I. SRIM input parameters for W and CoFeB (4:4:2). ρ is the bulk material density, E_D is the bulk atom displacement energy, E_L is the lattice energy, and U_0 is the surface atom binding energy. Each value was obtained from the reference and other values were used to deduce sputter yield and sputtered atom characteristics.^{34,35}

Type of SRIM calculation	ρ (g/cm ³)	U_0 (eV)	E_D (eV)	E_L (eV)	Ion incident energy (eV)
W	19.35	25	3	8.68	He: 150/ 250/ 350 Ar: 35/47/52
CoFeB (4:4:2)	7.80	Co: 25 Fe: 25 B: 25	Co: 3 Fe: 3 B: 3	Co: 4.43 Fe: 4.34 B: 5.73	He: 150/ 250/ 350 Ar: 35/47/52

Table II. Sputtering yields of Co, Fe, and B in amorphous CoFeB and W investigated by SRIM simulation program.

Incident Energy (eV)	$\langle S \rangle$ of W	$\langle S \rangle$ of Co in CoFeB	$\langle S \rangle$ of Fe in CoFeB	$\langle S \rangle$ of B in CoFeB
He	150	0.000	0.036	0.010
Ar	35	0.006	0.037	0.005
He	250	0.002	0.062	0.016
Ar	47	0.076	0.066	0.010
He	350	0.025	0.074	0.018
Ar	52	0.100	0.075	0.011

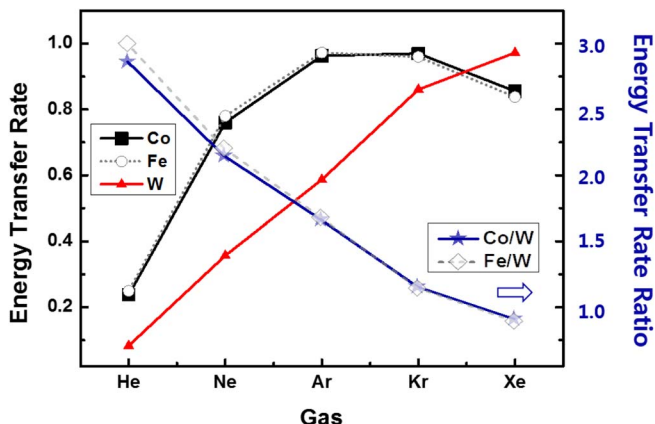


Figure 2. Energy transfer rates of Co, Fe and W by He, Ne, Ar, Kr and Xe and their ratios of (Co,Fe)/W estimated using Eq. 1.

Based on the simulation results, blank unit thin films related to MTJs were etched and the results were compared with the simulation results. Figure 3a shows the etch rates of materials related to MTJs such as MgO, CoPt, and CoFeB with W used as a hardmask material. Figure 3b shows the etch selectivities of the materials over W for etching using the ICP etcher with a bias voltage of -150 V for He and -35 V for Ar. To compare with previous etch results on magnetic materials, the etching of the materials at the bias voltage of -400 V with CO/NH₃ (1:3) was also investigated.³⁰

For the etching experiment, the same condition of 13.56 MHz source power of 700 W flow rate of 50 sccm, operating pressure of 7 mTorr, and room temperature were used for all materials. As shown in Fig. 3a, at -150 V of He and -35 V of Ar, the etch rates of CoFeB were similar at 5.14 and 5.06 nm/min, respectively; therefore, the simulation results of sputter yields in Table II could be confirmed experimentally. The etch rates of MgO and CoPt at -150 V of He and -35 V of Ar were also similar each other. For the etch selectivity measured by the experiment, as shown in Fig. 3b, the etch selectivity of CoFeB/W for -150 V He (4.39) was higher than that for -35 V Ar (0.93) similar to the simulation results in Table II and also in Fig. 3c even though the sputter yield ratios of CoFeB/W for simulation results were much higher than experimental results by showing ~ 600 for 150 V He and ~ 6.7 for 35 V Ar as mentioned above. The differences between the etch selectivity obtained by experiment and sputter yield ratio obtained by simulation appear to be related to the non-consideration of plasma potential, the energy distribution in the ion energy bombarding the substrate, and the gas impurity effect that could not be considered in the simulation. Especially, the lower etch selectivity obtained by the experiment is believed to be more related to a wide energy distribution of He ion incident to the materials surface. By using the He ions with a narrower energy distribution, higher etch selectivity of MTJ over the mask materials, therefore, more anisotropic etch profile of MTJ feature could be achieved. In general, it is known that the use of lower ion mass and lower rf bias power frequency tend to increase ion energy distribution incident to the substrate. By using a very high frequency (>30 MHz) rf bias power instead of a lower frequency (13.56 MHz) rf bias power as a next step, it is believed that a narrower He ion energy distribution, therefore, more selective MTJ etching can be obtained for the aggressive scaling of these MTJ features. However, even for now, the etch selectivities of CoFeB over W were still higher for -150 V He compared to -35 V Ar at the similar etch rates of MTJ materials. In the case of CO/NH₃ at -400 V, as shown in Figs. 3a and 3b, the etch rates of MgO, CoFeB, and CoPt were higher than that etched with -150 V He while the etch selectivities over W were a little lower than those etched with -150 V He. In the etching of magnetic materials related to MTJs by inert gases such as He and Ar, one of the serious problems is the sidewall redeposition of magnetic materials on the etched MTJ features due to the non-volatility of the sputter

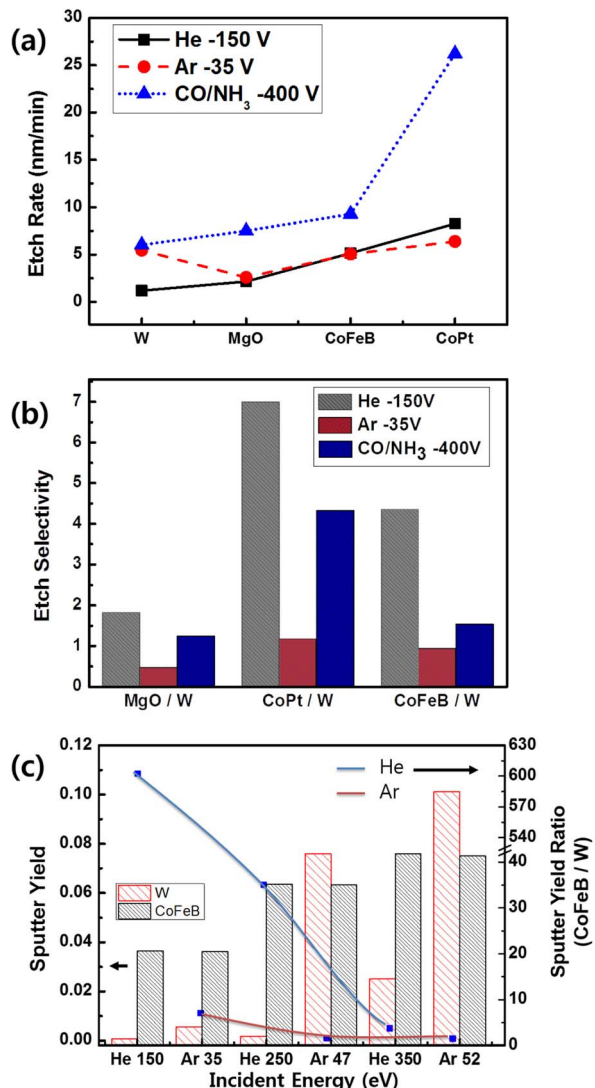


Figure 3. (a) Etch rates of magnetic material CoPt, CoFeB and mask material W, and barrier material MgO for each condition. (b) Etch selectivities of MgO/W, CoPt/W and CoFeB/W (c) Sputter yields and sputtering yield ratios between CoFeB/W obtained by the SRIM simulation shown in Table II.

etched materials. Using the SRIM simulation, the energy and angular distribution of the sputtered magnetic atoms by the sputter etching using He and Ar were investigated. Figures 4 and Figure 5 show the simulation results of the energy and angular distribution of sputtered Co in CoFeB and the angular probability density function (PDF) of sputtered Co by He and Ar, respectively. The black arrow indicates the direction of incident atom. The angular probability density function (PDF) of sputtered Co (Fig. 4b, Fig. 5b) reconfigured from Figs. 4a and Fig. 5a, respectively. The incident energies for the simulation were 150 eV for He and 35 eV for Ar. The simulation results of Fe were similar to those of Co, therefore, only the results of Co are shown in Fig. 4 and Fig. 5. As shown in Figs. 4 and 5 the sputtered Co atoms tend to have higher energy and higher ejection angle for 150 eV He than 35 eV Ar. The average ejection angles for 150 eV He and 35 eV Ar were 72.86° and 68.78° from the surface, respectively; therefore, the Co atoms were sputtered with higher angles by 150 eV He than 35 eV Ar. The etch profiles are generally affected by the etch selectivities of W mask over MTJ materials and redeposition of material on the sidewall of the etched features. The different sputter angles of magnetic materials during the sputter etching with He and Ar obtained in the simulation of Figs. 4 and 5 can be related to the degree of redeposition of magnetic materials during the etching of

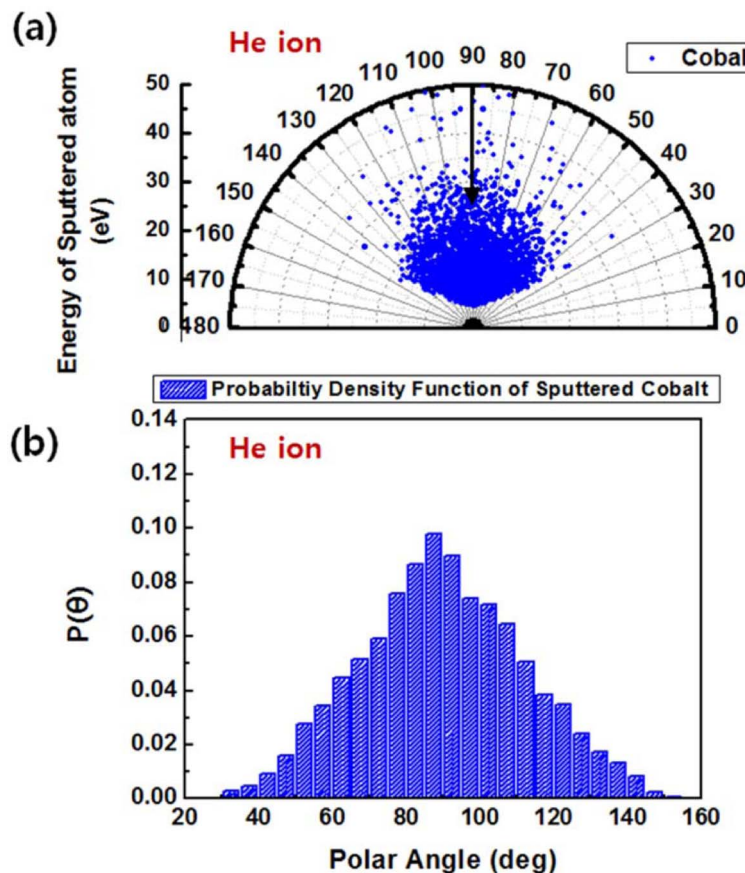


Figure 4. Energy and angular distribution of sputtered Co in CoFeB with He (a) and angular probability density function of sputtered Co atom with He (b). The incident energies of the simulation are 150 eV for He.

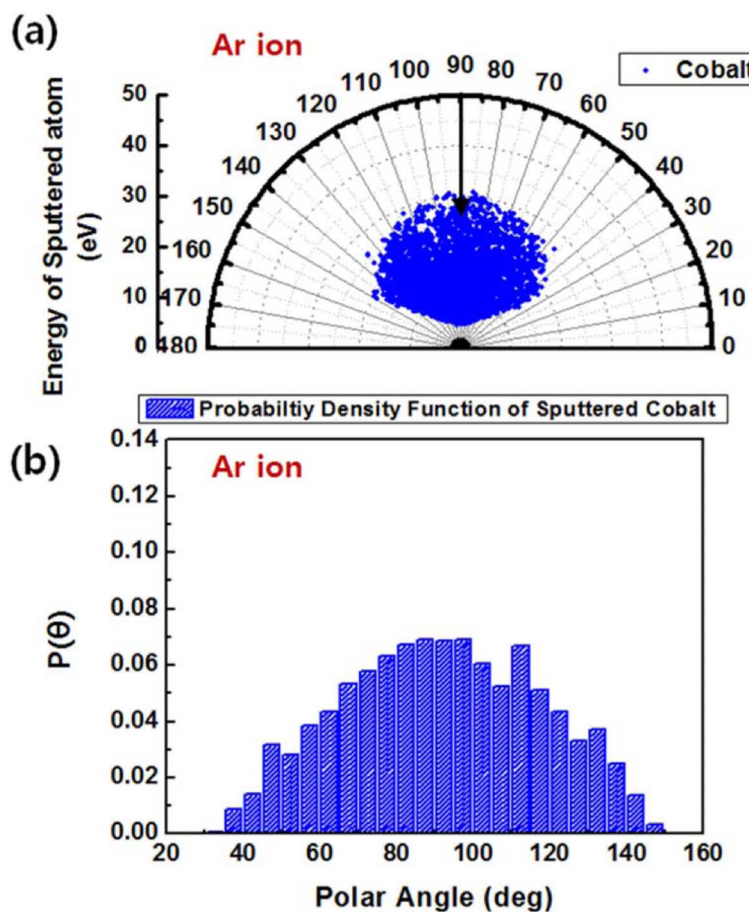


Figure 5. Energy and angular distribution of sputtered Co in CoFeB with Ar (a) and angular probability density function of sputtered Co atom with Ar (b). The incident energies of the simulation are 35 eV for Ar.

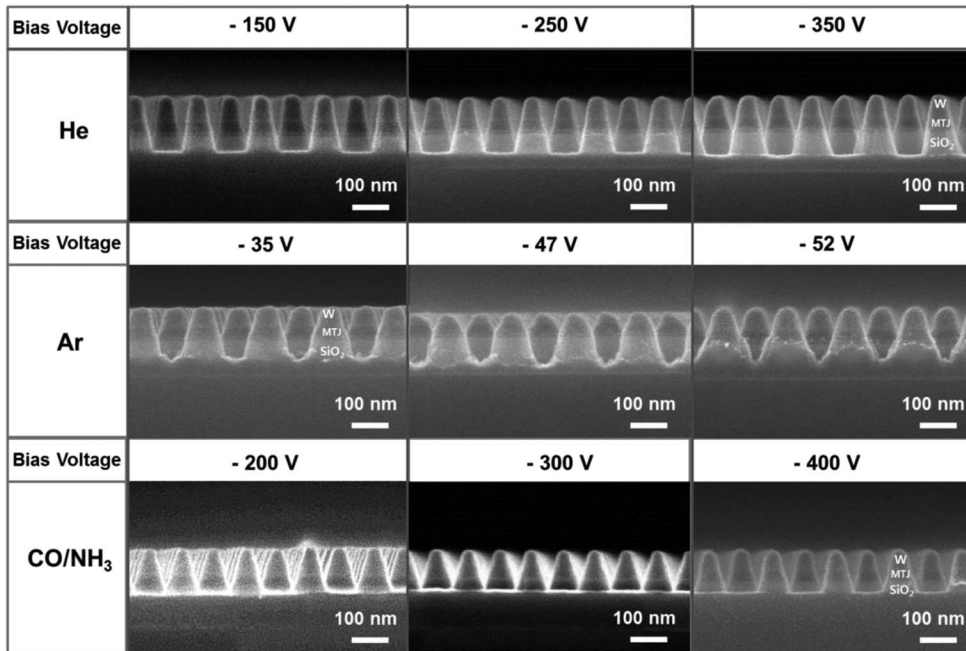


Figure 6. SEM etch profiles of the nanoscale patterned MTJ stack features composed of CoPt (10 nm)/MgO (1 nm)/CoFeB (10 nm) on Ta/SiO₂/silicon wafer. Patterned W (100 nm)/Ti (3 nm)/Ru (10 nm) was used. Also, to achieve similar etch depth, the etch time was varied for each condition.

nanoscale MTJ features, therefore, it may also affect the etch profiles and electrical short of MTJs.

Using the patterned MTJ sample, etch profiles were observed by field emission scanning electron microscopy (FE-SEM; Hitachi, S-4700) after the etching using He (-150 V/-250 V/-350 V), Ar (-35 V/-47 V/-52 V), and CO/NH₃ (-200 V/-300 V/-400 V) are shown in Fig. 6. For each etch condition, different etch times were used to maintain the same MTJ etch depth. Other etch conditions are the same as those used to etch the blank unit thin films. With Ar, the etch profile was not highly anisotropic due to the poor etch resistance of W over Ar and the severe redeposition of W on the surfaces of the MTJ materials, which was predicted in the SRIM simulation and the blank unit thin film etch test. The composition of CO:NH₃ (1:3) and the bias voltage ranging from -200 to -400 V were selected from the previous studies,³⁸ that show the anisotropic etch profiles with CO/NH₃ gas mixtures. As shown in Fig. 6, even though the etch depths are similar, the increase of bias voltage degraded the etch profile for all etch gases, due to the decreased etch selectivity of the magnetic materials over W as obtained by the SRIM results. The etch characteristics were similar to those by He ICP, even though the etch

profiles of CO/NH₃ were slightly worse than those etched using He ICP. As shown in Fig. 7, the sidewall angles of the MTJ stacks were 81° for He, 75° for Ar and 79° for CO/NH₃. Therefore, the most anisotropic MTJ etch profiles could be observed by etching using He as expected from the previous results.

To observe the possible redeposited material and residue on the etched MTJ features, the MTJ features etched using -150 V He and -400 V CO/NH₃ (shown in Fig. 6) were observed using transmission electron microscopy (TEM, ARM-200F). The results are shown in Figs. 8a and 8b for He and CO/NH₃, respectively. Due to the rough sidewall and the least anisotropic etch profile, no TEM images were taken for the MTJ features etched using Ar. As shown in Fig. 8, a more anisotropic etch profile could be observed for the MTJ feature etched by He. However, no sidewall redeposited material or residue could be clearly observed for the MTJ features etched with He or CO/NH₃, possibly due to the extreme thin thickness of the remaining residue material. Even though no noticeable sidewall redeposition or residue could be observed on the etched MTJ features, the MTJ features can be degraded by forming a very thin damaged layer or impurity layer, etc. during the etching.

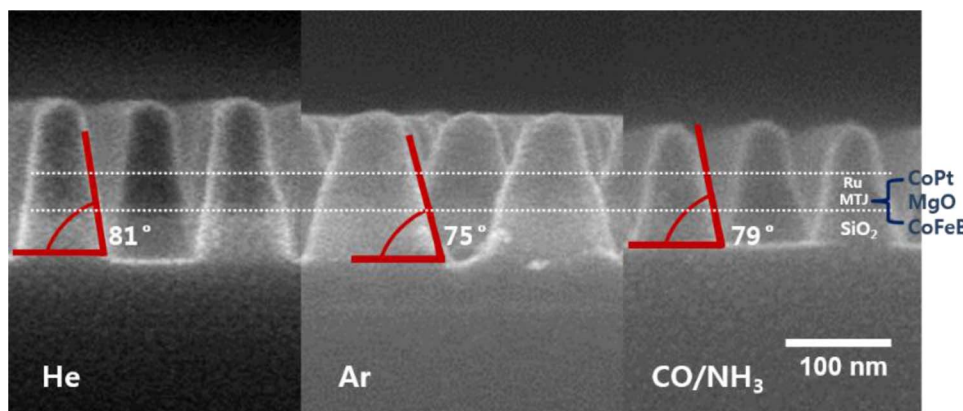


Figure 7. Magnified SEM images of the nanoscale patterned MTJ stack features for - 150 V He, - 35 V Ar, and - 400 V CO/NH₃ in Fig. 6.

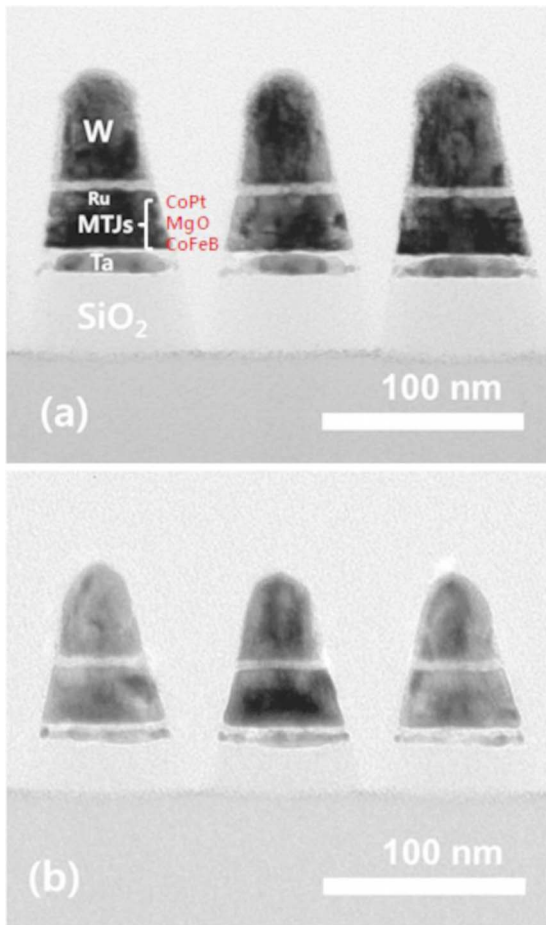


Figure 8. TEM images of patterned MTJ stack after the etching using bias voltage of (a) -150 V with He and (b) -400 V CO/NH_3 . All scale bars are 100 nm.

To investigate the magnetic degradation of the MTJ features after the etching, the magnetic properties of the MTJ features etched with -150 V He, -35 V Ar, and -400 V CO/NH_3 were investigated using a vibrating sample magnetometer (VSM; GMW, 3474-140); the results are shown in Fig. 9. As shown in Fig. 9, the etched MTJ features exhibited typical magnetic hysteresis loops with saturated magnetic moments (M_S); however, the M_S of MTJ etched by CO/NH_3

was 61.1% of that etched with Ar. The oxygen in the gas chemistry tends to form a thin oxide layer on the patterned sidewall of MTJ materials, which reduces the performance of the device. Therefore, even though no sidewall redeposited material, residue, or damage could be observed in Fig. 7, the MTJ features etched by CO/NH_3 appeared to be chemically damaged by forming a sidewall oxide on the surface. However, in the case of the MTJ feature etched with He, the M_S was about 92.3% of that with Ar was observed. A little smaller M_S for He compared to Ar could be related to the surface damage of MTJ due to deeper penetration of He by the high energy of the He-ions compared to Ar during the etching. (SRIM simulation showed that the penetration depth for 150 eV He into Co/Fe can be ~ 10 nm while that for 35 eV Ar is ~ 2.5 nm when ion is incident to the materials vertically) However, it is believed that, by having more anisotropic etching of MTJ, a less physical damage to the MTJ sidewall surface by He ion is expected by less penetration of He ion to the sidewall of the features.

Conclusions

The advantages of etching magnetic materials related to MTJs of STT-MRAM using He ions with the energy close to the hardmask sputter threshold energy as an alternative to Ar and other gas mixtures such as CO/NH_3 were investigated. Due to the higher etch selectivity of the magnetic material over W for He compared to Ar at similar etch rates of the magnetic materials, the etching of patterned MTJ with W hardmask using He exhibited a much better etch profile and less hardmask erosion than that using Ar, especially at an He ion energy close to the hardmask sputter threshold energy. The use of the CO/NH_3 gas mixture in the etching MTJ exhibited etch characteristics comparable to He. However, the CO/NH_3 gas mixture appeared to induce more magnetic degradation than the inert gases such as He and Ar due to the sidewall oxidation of the etched MTJ features. Therefore, it is believed that the etching of MTJ using He with the ion energy near the hardmask sputter threshold energy could be beneficial in obtaining highly anisotropic etch profiles without the formation of the sidewall redeposited materials and without significant electrical degradation of magnetic properties.

Acknowledgments

This research was supported by the (NRF-2016M3A7B4910429).

References

- V. V. Zhirnov, R. K. Cavin III, S. Menzel, E. Linn, S. Schmelzer, D. Braühaus, C. Schindler, and R. Waser, *Proc. IEEE*, **98**, 2185 (2010).
- Y. Huai, *AAPPS Bulletin*, **18**, 33 (2008).
- A. D. Kent and D. C. Worledge, *Nat. Nanotechnol.*, **10**, 187 (2015).
- S. Ikeda, K. Miura, H. Yamamoto, K. Mizunuma, H. Gan, M. Endo, S. Kanai, J. Hayakawa, F. Matsukura, and H. Ohno, *Nat. Mater.*, **9**, 721 (2010).
- J. Park, S. Kang, M. Jeon, M. S. Jhon, and G. Y. Yeom, *J. Electrochem. Soc.*, **158**, H (2011).
- X. Jiang, Q. Gu, F. Wang, J. Lv, Z. Ma, and G. Si, *Mater. Lett.*, **100**, 192 (2013).
- K. Kinoshita, H. Utsumi, K. Suemitsu, H. Hada, and T. Sugibayashi, *Jpn. J. Appl. Phys.*, **49**, 08JB02 (2010).
- J. Read, P. Braganca, N. Robertson, and J. Childress, *APL Mater.*, **2**, 046109 (2014).
- W. Boullart, D. Radisic, V. Paraschiv, S. Cornelissen, M. Manfrini, K. Yatsuda, E. Nishimura, T. Ohishi, and S. Tahara, *Proc. SPIE*, **8685**, (2013).
- K. Kinoshita, H. Honjo, S. Fukami, H. Sato, K. Mizunuma, K. Tokutome, M. Murahata, S. Ikeda, S. Miura, N. Kasai, and H. Ohno, *Jpn. J. Appl. Phys.*, **53**, 103001 (2014).
- K. C. Yang, S. W. Park, M. H. Jeon, V. P. Pham, D. Y. Lee, T. H. Shim, J. G. Park, and G. Y. Yeom, *Vacuum*, **127**, 82 (2016).
- E. J. O'Sullivan, M. J. Gajek, J. J. Nowak, S. L. Brown, M. C. Gaidis, G. Hu, J. Z. Sun, P. L. Trouilloud, D. W. Abraham, R. P. Robertazzi, W. J. Gallagher, and D. C. Worledge, *ECS Transactions*, **58**, 117 (2013).
- Y. Ohsawa, N. Shimomura, T. Daibou, Y. Kamiguchi, S. Shirotori, T. Inokuchi, D. Saida, B. Altansargai, Y. Kato, H. Yoda, T. Ohkubo, and K. Hono, *IEEE Trans. Magn.*, **52**, 3400803 (2016).
- D. Worledge, M. Gajek, D. Abraham, S. Brown, M. Gaidis, G. Hu, J. Nowak, E. J. O'Sullivan, R. Robertazzi, and J. Sun, *IEEE Int. Memory Workshop* (2012).

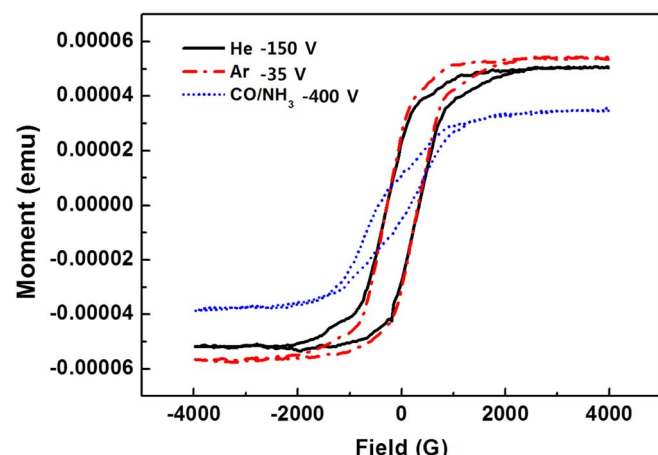


Figure 9. Minor magnetic hysteresis loops of patterned MTJ etched using He -150 V, Ar -35 V, and CO/NH_3 -400 V measured by VSM method.

15. X. Peng, S. Wakeham, A. Morrone, S. Axdal, M. Feldbaum, J. Hwu, T. Boonstra, Y. Chen, and J. Ding, *Vacuum*, **83**, 1007 (2009).
16. H. Gokan and S. Esho, *J. Vac. Sci. Technol.*, **A19**, 28 (1981).
17. J. Jeong and T. Endoh, *Jpn. J. Appl. Phys.*, **56**, 04CE09 (2017).
18. S. R. Min, H. N. Cho, K. W. Kim, Y. J. Cho, S. Choa, and C. W. Chung, *Thin Solid Films*, **516**, 3507 (2008).
19. M. Satake, M. Yamada, and E. Matsumoto, *J. Vac. Sci. Technol.*, **B34**, 061806 (2016).
20. I. Nakatani, *IEEE Trans. Magn.*, **32**, 4448 (1996).
21. M. H. Jeon, K. C. Yang, J. W. Park, D. H. Yun, K. N. Kim, and G. Y. Yeom, *J. Nanosci. Nanotechnol.*, **16**, 11823 (2016).
22. M. H. Jeon, K. C. Yang, J. W. Park, D. H. Yun, K. N. Kim, and G. Y. Yeom, *J. Vac. Sci. Technol.*, **B33**, 061212 (2015).
23. H. Honjo, S. Fukami, K. Ishihara, K. Kinoshita, Y. Tsuji, A. Morioka, R. Nebashi, K. Tokutome, N. Sakimura, M. Murahata, S. Miura, T. Sugibayashi, N. Kasai, and H. Ohno, *IEEE Trans. Magn.*, **50**, 1401904 (2014).
24. K. M. Wu, C. H. Huang, S. C. Lin, M. J. . Kao, M. J. Tsai, J. C. Wu, and L. Horng, *Phys. Stat. Sol. (a)*, **204**, 3934 (2007).
25. J. H. Jeong, T. Endoh, Y. Kim, W. K. Kim, and S. O. Park, *J. Appl. Phys.*, **115**, 17C727 (2014).
26. X. Gu, Y. Kikuchi, T. Nozawa, and S. Samukawa, *J. Phys. D: Appl. Phys.*, **47**, 322002 (2014).
27. N. Matsui, K. Mashimo, A. Egami, A. Konishi, O. Okada, and T. Tsukada, *Vacuum*, **66**, 479 (2002).
28. K. Sugiura, S. Takahashi, M. Amano, T. Kajiyama, M. Iwayama, Y. Asao, N. Shimomura, T. Kishi, S. Ikegawa, H. Yoda, and A. Nitayama, *Jpn. J. Appl. Phys.*, **48**, 08HD02 (2009).
29. K. Kinoshita, T. Yamamoto, H. Honjo, N. Kasai, S. Ikeda, and H. Ohno, *Jpn. J. Appl. Phys.*, **51**, 08HA01 (2012).
30. J. H. Jeong, T. Endoh, Y. Kim, W. Kim, and S. Park, *J. Appl. Phys.*, **115**, 17C727 (2014).
31. K. Watanabe, *ECS Transactions*, **3**, 137 (2007).
32. M. Satake and M. Yamada, *Jpn. J. Appl. Phys.*, **56**, 046202 (2017).
33. M. H. Jeon, H. J. Kim, K. C. Yang, S. K. Kang, K. N. Kim, and G. Y. Yeom, *Jpn. J. Appl. Phys.*, **52**, 05EB03 (2013).
34. P. Kumar, A. Ahmad, and M. Carrère, *Radiat. Eff. Defects Solids.*, **170**, 567 (2015).
35. D. Kirk, A. Kohn, K. B. Borisenko, C. Lang, J. Schmalhorst, G. Reiss, and D. J. J. Cockayne, *Phys. Rev. B*, **79**, 014203 (2009).
36. J. F. Ziegler, M. D. Ziegler, and J. P. Biersack, *Nucl. Instrum. Methods. Phys. Res. B*, **268**, 1818 (2010).
37. D. Rosenberg and G. Wehner, *J. Appl. Phys.*, **33**, 1842 (1962).
38. K. C. Yang, M. H. Jeon, and G. Y. Yeom, *Jpn. J. Appl. Phys.*, **54**, 01AE01 (2015).